Key Engineering Materials
ISSN: 1662-9795, Vol. 1047, pp 359-371

Submitted: 2026-01-22
Accepted: 2026-02-11
Online: 2026-04-13

Comparison between 2D and 3D Thermal Finite Element Models of Directed Energy Deposition

Gallo Calogero[1,a], Van Hulle Samuel[2,b], Tchoufang Tchuindjang Jérôme[3,c], Mertens Anne[3,d], Duchene Laurent[1,e*] and Habraken Anne Marie[1,f]

[1]Department ArGEnCo-MSM, University of Liège, Quartier Polytech 1, Allée de la Découverte 9, 4000 Liège, Belgium

[2]Aerospace and Mechanical Engineering Department, University of Liège, 4000 Liège, Belgium

[3]Department A&M–MMS, University of Liège, Quartier Polytech 1, allée de la Découverte 9, 4000 Liège, Belgium

[a]cgallo@uliege.be, [b]S.VanHulle@uliege.be, [c]j.tchuindjang@uliege.be, [d]anne.mertens@uliege.be, [e*]l.duchene@uliege.be, [f]anne.habraken@uliege.be

Keywords: M4 steel, additive manufacturing, DED, FE model, sensitivity analysis.

Abstract. Varying boundary conditions, such as convection, radiation, and contact thermal exchange parameters in Directed Energy Deposition (DED) process modeling, can significantly impact the predicted thermal fields [1] and final properties of a product. The current numerical study analyzes the effect of different boundary conditions on the temperature distribution during DED thanks to a 3D model of AISI M4 tool steel validated by an experimental campaign. It also confirms that a 2D FE model can already provide valuable trends about sensitivity of numerical results to boundary conditions. The accuracy and robustness of the 2D and 3D model predictions are analyzed. The temperature histories of a set of points at different heights in the clad and the melt pool dimensions provide experimental validation.

Introduction

Additive manufacturing processes represent a wide range of techniques that generate pieces, using material in a raw form (powder, welding cable, bar, liquid,…) [2–5]. Laser-Directed Energy Deposition (L-DED) is a technique using powder [6], which is guided by an argon flux at the laser focus. Its main application field is for the repair of pieces [7].

During the process, material is added layer by layer. The temperature field presents a complex evolution due to the modification of the topology of the specimen. So, each layer has a different cooling behavior, which leads to different cooling rates. This temperature history directly influences the melt pool and the heat-affected zone (HAZ), which are two important characteristics determining the final part properties [8–10].

Due to the displacement of the heat source, the boundary conditions evolve with time in this kind of process [11]. The argon flux is also modified due to the displacement of the laser, which influences the heat evacuation due to convection [12]. The high level of energy density creates non-uniform radiation heat evacuation in addition to the laser-powder interaction which generates multiple reflections of the laser-beam [13]. Furthermore, a part of the laser power is directly reflected. In a small enclosure, this can cause a non-uniform temperature distribution of the environment [14].

The importance of modeling the process is crucial due to the high complexity of the additive manufacturing techniques. A lot of process parameters can affect the results and generate different kinds of defects. Such issues can happen at the melt pool level (balling, keyholes, porosities,…) [15] or at the layer level (sagging, deformation, surface finish,…) for instance [16–18].

M4 steel was selected for the studied deposit. This choice leads to a major difference with mostly used materials like stainless steel or titanium (TA6V) [19]. Indeed, it prevents the printing of a large part due to the high level of residual stress generating the failure of the printing. The substrate needs to be preheated to reduce the thermal gradient [20]. If it is not well considered, cracks can appear during the cooling with material phase transformations generating additional stress [21].

Experimental Setup

The 5-axis Irepa Laser Cladding system with a Nd-YAG laser of maximum power capacity of 2000 W from Sirris Research Centre is used. It is schematically described in **Fig. 1** [22]. The laser has a wavelength of 1064 µm and operates continuously. The metal powder is injected with an angle of 38 to 45 degrees while the angle of the nozzle is 90°. The laser power has a top-hat energy distribution with a diameter of 1400 µm (it is considered constant in the simulations [23]). A home-made protection cap filled with argon avoids contamination of the melt pool by interstitial elements such as oxygen or nitrogen [24]. The oxygen concentration within the protective atmosphere is below 10 ppm. The substrate of 40 mm height and 95 mm diameter is made of 42CrMo4 steel and preheated to 400 °C to prevent cracks in the deposit. The substrate top is surrounded by a 10 mm aluminium plate while at the bottom, steel and aluminium plates are present, helping to diffuse heat. However, this configuration results in the appearance of a thermal contact resistance (TCR) between the substrate and the steel plate, as no pressure is applied to bond them together. That causes a reduction of the heat flux between both pieces [25]. The induction power supply is a COBES shuJuno 12kW working at 139kHz and is positioned around the substrate.

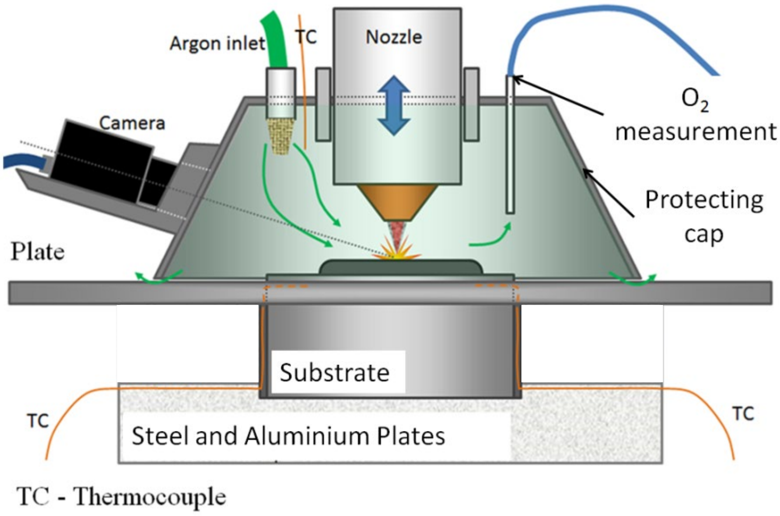

Fig. 1. Scheme of laser cladding equipment used for manufacturing the studied specimen.

The laser path uses a zigzag strategy with an offset of half a track between two successive layers, with a total of 8 tracks per layer and an idle time of 7.5 seconds. These parameters produce a clad of 43.35 x 13.375 x 23.16mm^3 (length x width x height, which corresponds to axes X, Y and Z), see **Fig. 2**.

Four thermocouples are placed 5 mm below the surface at different positions (described in **Fig. 2**). An additional one is placed below the steel plate at the center. These thermocouples collect data during the process, which is composed of 3 different stages:

- Preheating: The induction heater is set at 1450W for approximately 45 minutes. Once the goal temperature (700K at the thermocouples in the substrate) is reached, the power is reduced to 250W for the rest of the process. Once the temperature has cooled down to 680K, the preheating is finished and the cladding starts.
- Cladding: The laser and the powder flux are turned on, to print the clad part the nozzle follows the predefined path.
- Cooling: At the cladding end, the laser and the powder flux are turned off. However, the induction heater remains active for one hour to prevent excessive cooling rates until the temperature has cooled down to 500K.

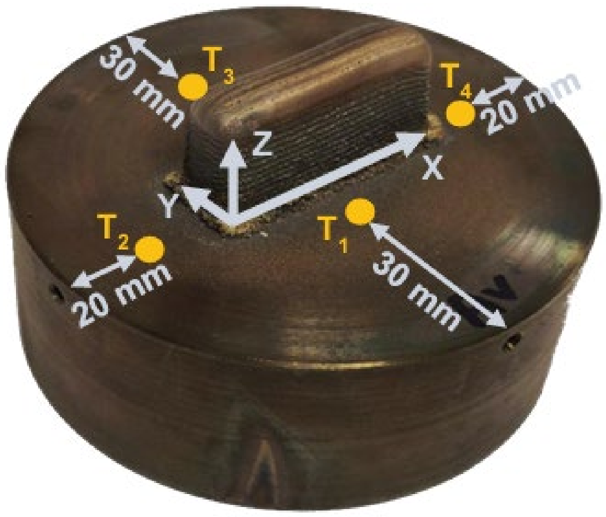

Fig. 2. Sample printed with the axis system defined and location of the thermocouples.

The parameters used for the cladding are described in **Tab. 1** below:

Table 1. DED manufacturing process parameters.

Laser power	1100 W
Scan speed	460 mm/min
Powder mass flux	79.3 mg/s
Argon flux	2.5 L/min

3D thermal FE model validation

The model uses Metafor software with nonlinear finite element [26] and is based on the work of [27]. The DED simulations rely on solid Finite Element (FE) using the birth element technique. The Marangoni effect was considered by multiplying the conductivity above the liquidus temperature by a factor 4 [28]. The TCR was modeled by reducing the conductivity of one layer of 1mm high at the bottom of the substrate. This TCR conductivity was assumed constant during each stage but different from one stage to another. Indeed, the application of the induction and laser heating implies thermo-mechanical deformation of the contact zone between the substrate and the plate which are different at each manufacturing stage, resulting in different TCR values.

Convection is modeled using a linear temperature dependence, assuming that the temperature distribution varies with distance from the laser spot, with the temperature decreasing as the distance increases, as presented by [12]. Emissivity is considered uniform and constant, except when the temperature is above the evaporation temperature (3084 K). The emissivity is then drastically increased to model the evaporation heat loss mechanism.

The simulation was validated on the temperature measured by thermocouple T_4 (placed in the substrate **Fig. 2**) and by the thermocouple measurement below the plate for the 3 different manufacturing stages (preheating, cladding and cooling). The 3 process steps are simulated by a single input material data set and adapted boundary conditions in Metafor. The comparison is presented in **Fig. 3** and **Fig. 4** respectively.

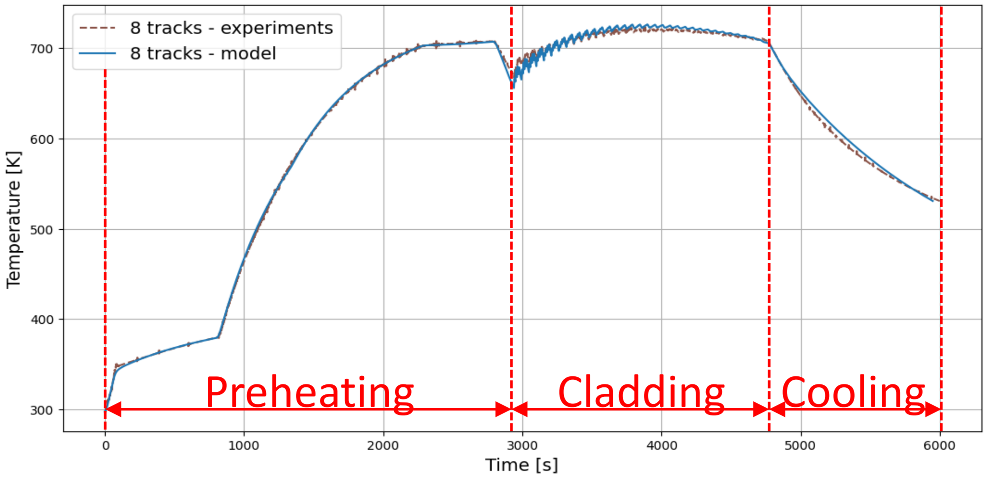

Fig. 3. Predicted and measured temperature curves for the thermocouple T_4 for the printing of an 8 tracks specimen.

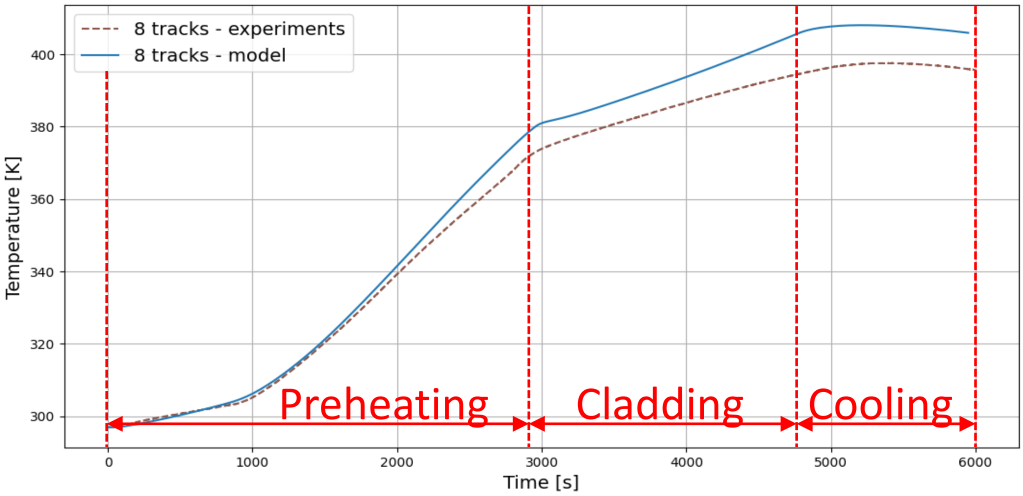

Fig. 4. Predicted and measured temperature curves for the thermocouple below the plate for the printing of an 8 tracks specimen.

2D FE model principle

This model consists of approximating the temperature field of the center plane of the clad as being representative of any thin plane of the clad. Therefore, only the center plane is explicitly modelled and tracks built out of this plane are neglected. It means that only the center track is printed, so the time needed for a layer becomes the time needed for a track. Another consequence of this 2D assumption is that no transversal heat flux exists (perpendicular to the middle plane).

It leads to a 2D model with strong assumptions, that has already been validated for bulk samples (27 tracks and 36 layers) [29]. It can generate good results but needs calibration with non-physical value of some parameters, which explains the model sensitivity to the setup variation and its poor predictive capabilities.

Despite these drawbacks, the model offers the advantage of being efficient by reducing the CPU time required for a simulation by approximately a factor of 100. The model is explained in details in [1].

Limitations

As explained in the introduction, the preheating of the substrate is one of the key challenges to prevent cracks event during the manufacturing process. To avoid the apparition of them in post-treating [30] an extensive numerical campaign was performed, it could demonstrate that the procedure was not well-adapted. Due to an insufficient consideration of the skin effect, the induction heater operates at a high frequency, resulting in a penetration depth of approximately 0.1 mm [31]. This phenomenon led to an overestimation of the temperature field by assuming that the temperature measured at the thermocouple was uniform. A deep FE 3D analysis has shown that it was not the case (**Fig. 5**). So, a new preheating procedure has been applied with a higher target temperature to prevent the risk of temperature drop below the martensitic start temperature, see **Tab. 2**.

Table 2. Preheating parameters.

	Initial procedure [1]	Final procedure
Induction power during preheating	1450W	550W
Preheating time	5 minutes	45 minutes
Induction power during cladding	From 550 to 50W	100W
Goal temperature	300°C	400°C

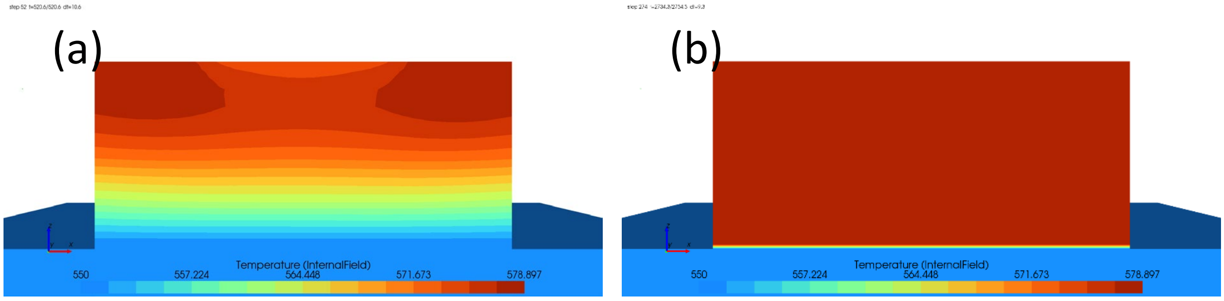

Fig. 5. Predicted thermal fields at the end of the preheating in the substrate - (a) for the initial procedure [1] (b) for the final procedure.

The excess of heat brough in the model due to the overestimation of the preheating was compensated by the lack of TCR in the model, which means that the model finally cools down the substrate more intensively than the reality. So, the current study goal was to ensure the good consistency of the 2D model and confirm it with a more physical 3D model.

Sensitivity Analysis

In [1], the sensitivity was defined as :

$$S_f = \left(\frac{\frac{f(BC(x^*)) - f(BC(x))}{f(BC(x))}}{\frac{x^* - x}{x}} \right) \tag{5}$$

S_f is the sensitivity to the parameter x, which belongs to a set of values representing the boundary conditions (BC), x is the identified value, x^* is the perturbed condition and f defines the FE prediction values. Due to the low amplitude of the perturbation, high simulation accuracy is required with small-time steps.

Three different Point Of Interest (POI) were studied. They are positioned at the center of the clad, at 50, 75 and 100% of the clad height, as shown in **Fig. 6**. The distance from the edges is large enough to avoid edge effects allowing to investigate the behavior of a stationary melt pool and the cooling rates. Two different cooling rates can be defined to characterize the cooling, both are described in **Fig. 7** (see also [1]):

- The average cooling rate: it determines the average cooling rate between the maximum temperature for a layer, and the smallest one.
- The liquidus-solidus cooling rate: it gives the cooling rate between the liquidus and the solidus temperatures. If the liquidus temperature is not reached, the highest temperature is considered.

Both cooling rates are calculated from the first four temperature peaks in the thermal history of each point of interest (POI). These peaks correspond to the four successive layers associated with each point and represent the primary driving force for metallurgical transformations due to their significant temperature gradients.

Thanks to the 2D and 3D process simulations a sensitivity coefficient was calculated for 5 different boundary parameters, the laser power absorbed, the convection coefficients of the clad and the substrate, the emissivity coefficients of the clad and the substrate by applying small perturbations on the set of parameter (see **Tab. 3**).

During the simulations, the melt pool depth is defined by measuring the greatest distance between the top of the clad and the point where the temperature is equal to the solidus temperature (1503K) as shown in **Fig. 8**. In this study, we focused on the melt pool depth of the three POI.

Table 3. Parameters used for the sensitivity analysis.

Perturbed parameter sets	Power absorbed β [/]	h_{clad} (at 300K and 2500K) [W/m^{2}K]	ε_{clad}[/]	$h_{substrate}$ [W/m^{2}K]	$\varepsilon_{substrate}$ [/]
Original set	0.23	20 - 70	0.65	20	0.65
Perturbed β	0.23023	20 - 70	0.65	20	0.65
Perturbed h_{clad}	0.23	20.02 – 70.07	0.65	20	0.65
Perturbed ε_{clad}	0.23	20 - 70	0.65065	20	0.65
Perturbed h_{substr}	0.23	20 - 70	0.65	20.02	0.65
Perturbed ε_{substr}	0.23	20 - 70	0.65	20	0.65065

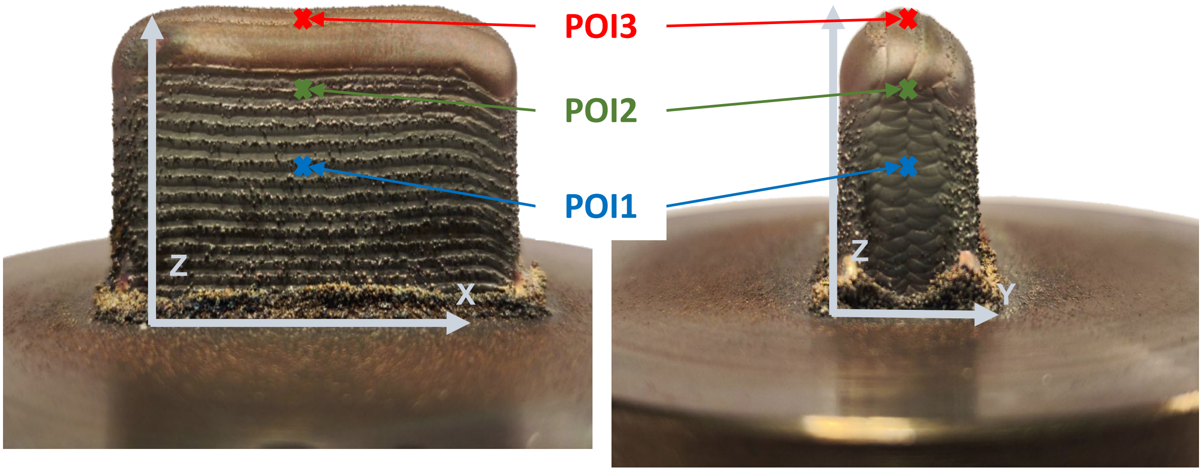

Fig. 6. Position of the different POI.

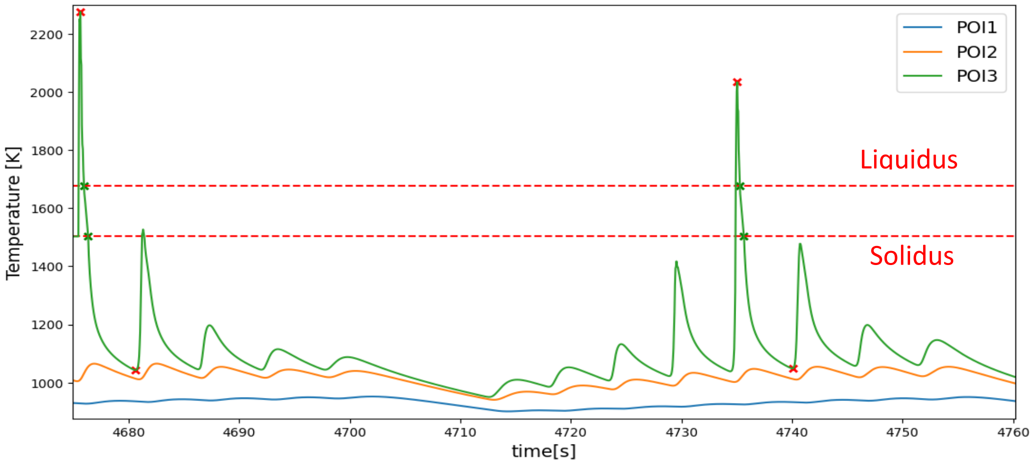

Fig. 7. Predicted temperature curves of the 3D model of the POI and positions used to calculate the cooling rates (red crosses for the average cooling rates and green ones for the entrance and exit in the liquidus solidus zone).

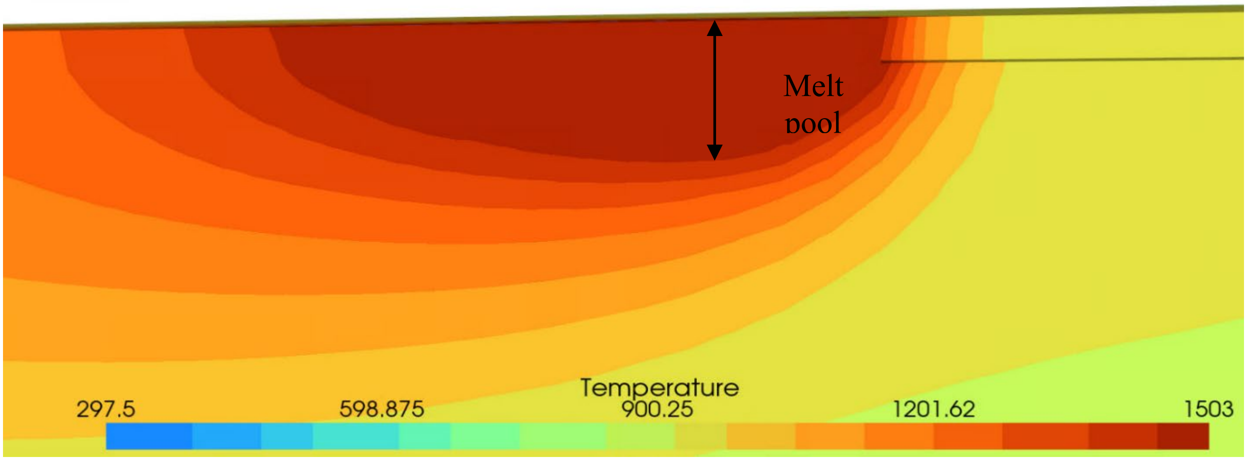

Fig. 8. Melt pool prediction for the 3D FE model.

Discussion

The sensitivities of the melt pool depth for both models are given in the next figures (in **Fig. 9**, **Fig. 10**).

Comparing the sensitivity of the melt pool depth with the results of both models (**Fig. 9**, **Fig. 10**) confirm the ability of the simplified model to capture the correct physical trends despite the 2D assumptions. The sensitivity of each parameter is going in the expected direction for both models:

- Increasing the laser power increases the melt pool depth.
- Increasing the heat evacuation parameters increases heat exchange and so reduces the melt pool depth.

Note that the 2D model tends to overestimate the effect of convection relative to radiation. In contrast, the 3D model captures these phenomena more realistically, allowing each contribution to be quantified more accurately. Considering the physical mechanisms at play in the melt pool, this confirms that radiation dominates over convection, as the melt pool contains the highest temperature regions.

The Z-position of each POI determines the thermal resistance between the point and the heat sink (substrate), the higher the point the higher the thermal resistance (considering the representation of a slice of material by an equivalent thermal resistance [32]). As additional layers are built, heat progressively accumulates. This effect is evidenced by the growth of the $S_{meltpool}$ from POI1 to POI3 (**Fig. 9**). This evolution is not well caught in the 2D model (**Fig. 10**) due to the non-representation of the out of plane heat exchanges, indeed this representation assumes no transversal leak which is a strong assumption for additive manufacturing process.

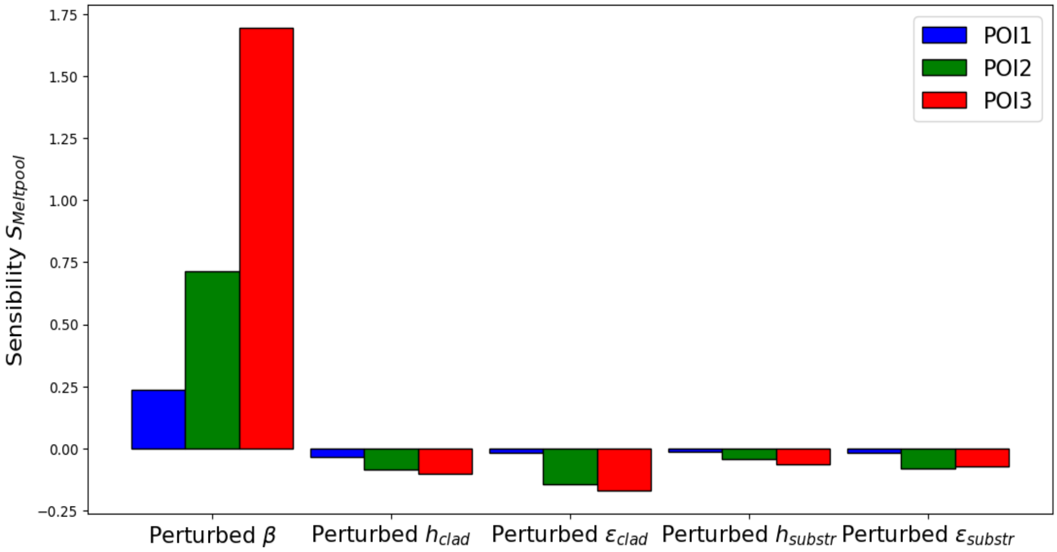

Fig. 9. Sensitivity of the melt pool depth computed with the 3D simulations.

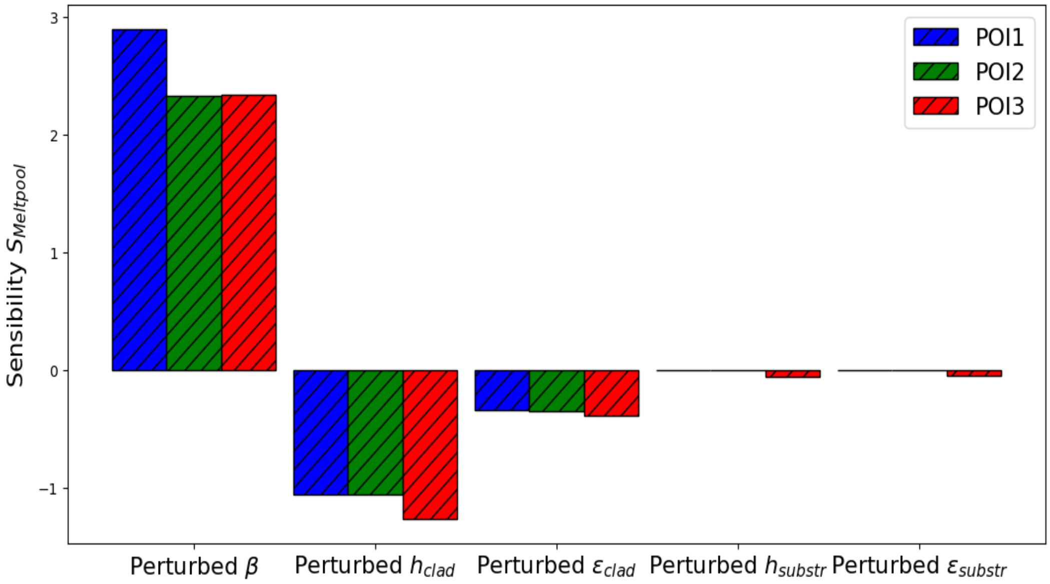

Fig. 10. Sensitivity of the melt pool depth for the 2D model. From [1].

The sensitivities of the cooling rates for both models are presented in the following figures (in **Fig. 11**, **Fig. 12**, **Fig. 13**, **Fig. 14**). Analysis shows that increasing the heat evacuation parameters leads to higher cooling rates as expected.

Comparing the results with the original study [1], this demonstrates that the 2D model cannot accurately estimate the impact of each contribution, particularly due to an overestimation of the effect of the convection. This is likely due to the high value of convection used to calibrate the 2D model with the experiment results and compensate the 2D assumption, which particularly avoids transversal heat flux. A 2D simulation can be seen as meta model with poor physical validation but providing anyway correct trends for selecting the main parameters affecting the melt pool or the cooling rates. The latter are important for the microstructure predictions.

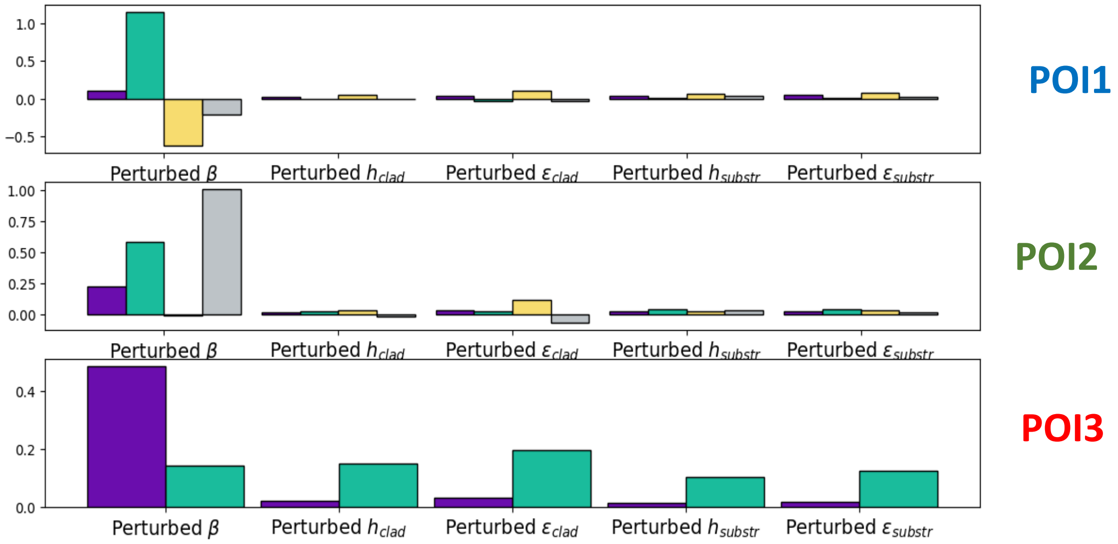

Fig. 11. Sensitivity of the average cooling rates computed with the 3D simulations.

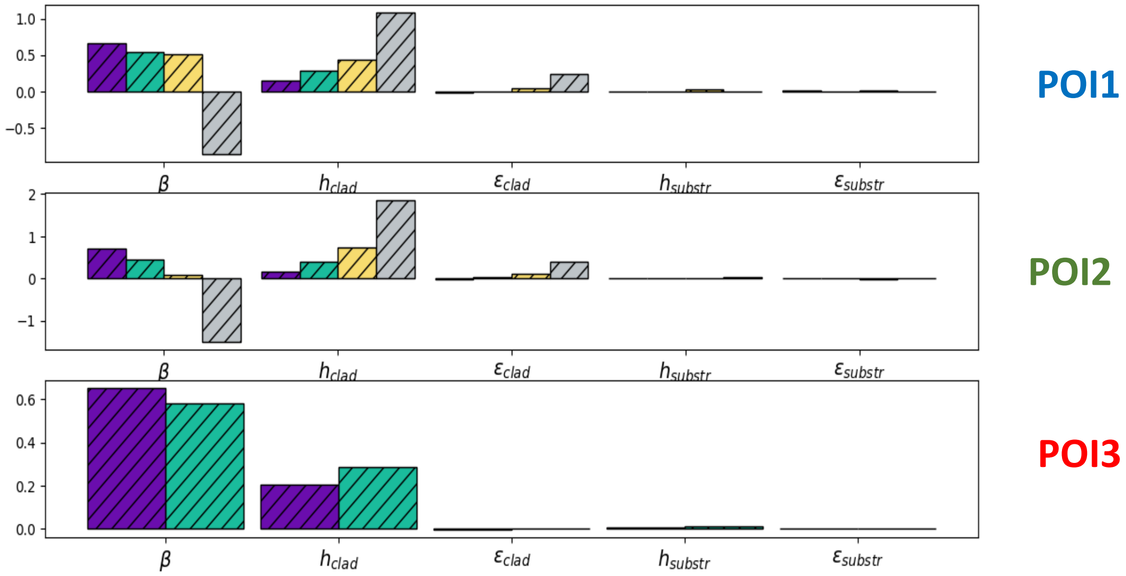

Fig. 12. Sensitivity of the average cooling rates for the 2D model. From [1].

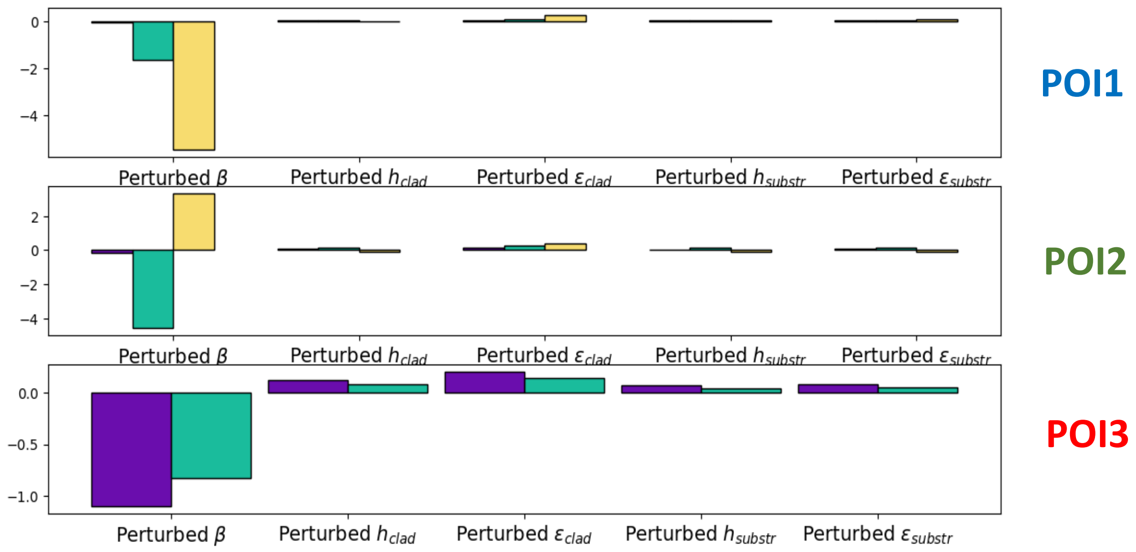

Fig. 13. Sensitivity of the liquidus-solidus cooling rates computed with the 3D simulations.

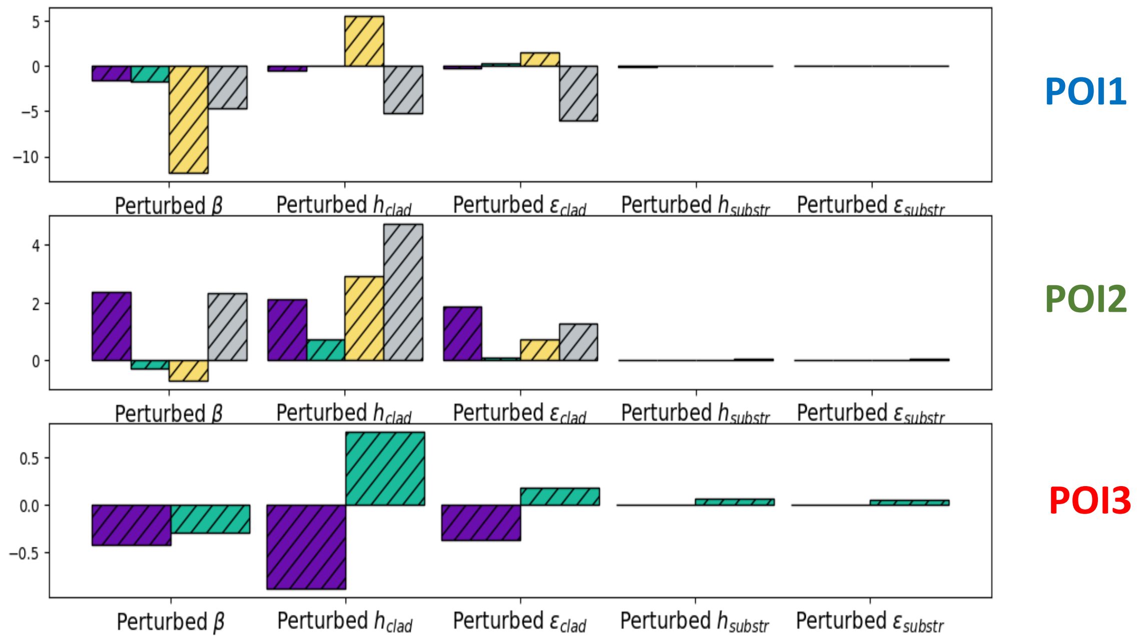

Fig. 14. Sensitivity of the liquidus-solidus cooling rates for the 2D model. From [1].

Conclusion

An experimental campaign allowed to produce a M4 clad sample. 3D and 2D FE models have been developed and validated on two different thermocouples and one thermocouple respectively.

The sensitivity analysis could validate the good behavior of the 3D FE model on the evaluation of the thermal field on local aspects (melt pool depth or cooling rates) and on the evolutions obtained along the Z axis, despite its assumptions, such as solid-state elements, convection coefficient estimation and TCR representation.

The comparison between this analysis and previous results demonstrates that the 2D model can give good results with limitations on trends observed due to the lack of physical meaning of this method.

Future Work

The same sensitivity analysis could be done with a specimen more representative of bulk component, as it was done in 2D. This could give the evolution of the sensitivities in function of the dimensions of the sample.

Acknowledgment

The mesh has been generated thanks to Gmsh [33].The FE models are developped on Lagamine [34] and Metafor [26].
As research director of F.R.S.-FNRS, A.M. Habraken thanks the Fund for Scientific Research for financial support. M4 experiments were funded thanks to two different FNRS F.R.S. Grants [PDRT.0039.14] Grant, Lasercladding and [CDR J.0080.21 EXP] 4 AM Digital tool for Microstructure. Collaboration with Chile is supported by the 7ème Commission mixte permanente Wallonie-Bruxelles/Chili 2023-2025 (RI 02).
The authors would also like to thank Raoul Carrus and Sirris Research Centre for providing the support and facilities of the laser cladding machine.

References

[1] Gallo, C.; Duchêne, L.; Quy Duc Pham, T.; Jardin, R.; Tuninetti, V.; Habraken, A.-M. Impact of Boundary Parameters Accuracy on Modeling of Directed Energy Deposition Thermal Field. Metals **2024**, 14, 173, doi:10.3390/met14020173.

[2] Svetlizky, D.; Zheng, B.; Vyatskikh, A.; Das, M.; Bose, S.; Bandyopadhyay, A.; Schoenung, J.M.; Lavernia, E.J.; Eliaz, N. Laser-Based Directed Energy Deposition (DED-LB) of Advanced Materials. Mater. Sci. Eng. A **2022**, 840, 142967, doi:10.1016/j.msea.2022.142967.

[3] Horgar, A.; Fostervoll, H.; Nyhus, B.; Ren, X.; Eriksson, M.; Akselsen, O.M. Additive Manufacturing Using WAAM with AA5183 Wire. J. Mater. Process. Technol. **2018**, 259, 68–74, doi:10.1016/j.jmatprotec.2018.04.014.

[4] Mishra, R.S.; Haridas, R.S.; Agrawal, P. Friction Stir-Based Additive Manufacturing. Sci. Technol. Weld. Join. **2022**, 27, 141–165, doi:10.1080/13621718.2022.2027663.

[5] Sukhotskiy, V.; Vishnoi, P.; Karampelas, I.H.; Vader, S.; Vader, Z.; Furlani, E.P. Magnetohydrodynamic Drop-on-Demand Liquid Metal Additive Manufacturing: System Overview and Modelling.; June 2018.

[6] DebRoy, T.; Wei, H.L.; Zuback, J.S.; Mukherjee, T.; Elmer, J.W.; Milewski, J.O.; Beese, A.M.; Wilson-Heid, A.; De, A.; Zhang, W. Additive Manufacturing of Metallic Components – Process, Structure and Properties. Prog. Mater. Sci. **2018**, 92, 112–224, doi:10.1016/j.pmatsci.2017.10.001.

[7] Piscopo, G.; Iuliano, L. Current Research and Industrial Application of Laser Powder Directed Energy Deposition. Int. J. Adv. Manuf. Technol. **2022**, 119, 6893–6917, doi:10.1007/s00170-021-08596-w.

[8] Wang, J.; Zhu, R.; Liu, Y.; Zhang, L. Understanding Melt Pool Characteristics in Laser Powder Bed Fusion: An Overview of Single- and Multi-Track Melt Pools for Process Optimization. Adv. Powder Mater. **2023**, 2, 100137, doi:10.1016/j.apmate.2023.100137.

[9] Mertens, A.; Delahaye, J.; Dedry, O.; Vertruyen, B.; Tchuindjang, J.T.; Habraken, A.M. Microstructure and Properties of SLM AlSi10Mg: Understanding the Influence of the Local Thermal History. Procedia Manuf. **2020**, 47, 1089–1095, doi:10.1016/j.promfg.2020.04.121.

[10] Liang, A.; Pey, K.S.; Polcar, T.; Hamilton, A.R. Effects of Rescanning Parameters on Densification and Microstructural Refinement of 316L Stainless Steel Fabricated by Laser Powder Bed Fusion. J. Mater. Process. Technol. **2022**, 302, 117493, doi:10.1016/j.jmatprotec.2022.117493.

[11] Keeley, W.; Turner, R.; Mitchell, B.; Warnken, N. A Development of the Rosenthal Equation for Predicting Thermal Profiles During Additive Manufacturing. Thermo **2025**, 5, 16, doi:10.3390/thermo5020016.

[12] Gouge, M.F.; Heigel, J.C.; Michaleris, P.; Palmer, T.A. Modeling Forced Convection in the Thermal Simulation of Laser Cladding Processes. Int. J. Adv. Manuf. Technol. **2015**, 79, 307–320, doi:10.1007/s00170-015-6831-x.

[13] Piscopo, G.; Atzeni, E.; Saboori, A.; Salmi, A. An Overview of the Process Mechanisms in the Laser Powder Directed Energy Deposition. Appl. Sci. **2022**, 13, 117, doi:10.3390/app13010117.

[14] Lia, F.; Park, J.; Tressler, J.; Martukanitz, R. Partitioning of Laser Energy during Directed Energy Deposition. Addit. Manuf. **2017**, 18, 31–39, doi:10.1016/j.addma.2017.08.012.

[15] Jiang, H.-Z.; Li, Z.-Y.; Feng, T.; Wu, P.-Y.; Chen, Q.-S.; Feng, Y.-L.; Chen, L.-F.; Hou, J.-Y.; Xu, H.-J. Effect of Process Parameters on Defects, Melt Pool Shape, Microstructure, and Tensile Behavior of 316L Stainless Steel Produced by Selective Laser Melting. Acta Metall. Sin. Engl. Lett. **2021**, 34, 495–510, doi:10.1007/s40195-020-01143-8.

[16] Gao, X.; Okigami, F.; Avedissian, N.; Zhang, W. An Experimental and Modeling Study on Warping in Additively Manufactured Overhang Structures. Addit. Manuf. **2024**, 81, 104017, doi:10.1016/j.addma.2024.104017.

[17] Haribaskar, R.; Kumar, T.S. Defects in Metal Additive Manufacturing: Formation, Process Parameters, Postprocessing, Challenges, Economic Aspects, and Future Research Directions. 3D Print. Addit. Manuf. **2024**, 11, e1629–e1655, doi:10.1089/3dp.2022.0344.

[18] Islam, S.A.; Hao, L.; Javaid, Z.; Xiong, W.; Li, Y.; Jamil, Y.; Chen, Q.; Han, G. Surface Roughness of Interior Fine Flow Channels in Selective Laser Melted Ti-6Al-4V Alloy Components. Micromachines **2024**, 15, 348, doi:10.3390/mi15030348.

[19] Jandyal, A.; Chaturvedi, I.; Wazir, I.; Raina, A.; Ul Haq, M.I. 3D Printing – A Review of Processes, Materials and Applications in Industry 4.0. Sustain. Oper. Comput. **2022**, 3, 33–42, doi:10.1016/j.susoc.2021.09.004.

[20] Shim, D.-S.; Baek, G.-Y.; Lee, E.-M. Effect of Substrate Preheating by Induction Heater on Direct Energy Deposition of AISI M4 Powder. Mater. Sci. Eng. A **2017**, 682, 550–562, doi:10.1016/j.msea.2016.11.029.

[21] Karalis, D.G.; Pantelis, D.I.; Papazoglou, V.J. Transient Stress of Steel Phase Transformation and Transformation-Induced Fatigue. Theor. Appl. Fract. Mech. **2010**, 54, 37–43, doi:10.1016/j.tafmec.2010.06.013.

[22] Jardin, R.T.; Tuninetti, V.; Tchuindjang, J.T.; Hashemi, N.; Carrus, R.; Mertens, A.; Duchêne, L.; Tran, H.S.; Habraken, A.M. Sensitivity Analysis in the Modelling of a High Speed Steel Thin-Wall Produced by Directed Energy Deposition. Metals **2020**, 10, 1554, doi:10.3390/met10111554.

[23] Liu, S.; Zhang, Y.; Kovacevic, R. Numerical Simulation and Experimental Study of Powder Flow Distribution in High Power Direct Diode Laser Cladding Process. Lasers Manuf. Mater. Process. **2015**, 2, 199–218, doi:10.1007/s40516-015-0015-2.

[24] Dinovitzer, M.; Chen, X.; Laliberte, J.; Huang, X.; Frei, H. Effect of Wire and Arc Additive Manufacturing (WAAM) Process Parameters on Bead Geometry and Microstructure. Addit. Manuf. **2019**, 26, 138–146, doi:10.1016/j.addma.2018.12.013.

[25] Madhusudana, C.V. Thermal Contact Conductance; Mechanical Engineering Series; Springer International Publishing: Cham, 2014; ISBN 978-3-319-01275-9.

[26] Documentation [Metafor] Available online: http://metafor.ltas.ulg.ac.be/dokuwiki/doc/user/start (accessed on 12 December 2025).

[27] Laruelle, C.; Boman, R.; Papeleux, L.; Ponthot, J.-P. Element Activation Strategy for Additive Manufacturing, Based on the Element Deletion Algorithm.; May 27 2019.

[28] Nikam, S.H.; Quinn, J.; McFadden, S. A Simplified Thermal Approximation Method to Include the Effects of Marangoni Convection in the Melt Pools of Processes That Involve Moving Point Heat Sources. Numer. Heat Transf. Part Appl. **2021**, 79, 537–552, doi:10.1080/10407782.2021.1872257.

[29] Jardin, T.; Antonio, R. Finite Element Thermal Analysis towards Microstructure Improvement in Directed Energy Deposition of High Speed Steel, ULiège - University of Liège [Département ArGEnCo], Liège, Belgium, 2024.

[30] Jardin, R.T.; Tuninetti, V.; Tchuindjang, J.T.; Duchêne, L.; Hashemi, N.; Tran, H.S.; Carrus, R.; Mertens, A.; Habraken, A.M. Optimizing Laser Power of Directed Energy Deposition Process for Homogeneous AISI M4 Steel Microstructure. Opt. Laser Technol. **2023**, 163, 109426, doi:10.1016/j.optlastec.2023.109426.

[31] Callebaut, J. Guide Power Quality – Section 7 : Efficacité énergétique - Chauffage par induction; European Copper Institute, 2007.

[32] Mobedi, M.; Gediz Ilis, G. Fundamentals of Heat Transfer: An Interdisciplinary Analytical Approach; Springer Nature Singapore: Singapore, 2023; ISBN 978-981-99-0956-8.

[33] Geuzaine, C.; Remacle, J. Gmsh: A 3-D Finite Element Mesh Generator with Built-in Pre- and Post-processing Facilities. Int. J. Numer. Methods Eng. **2009**, 79, 1309–1331, doi:10.1002/nme.2579.

[34] Start [Lagamine] Available online: http://www.lagamine.uliege.be/dokuwiki/doku.php (accessed on 12 December 2025).